A new method to model X-ray scattering from random rough surfaces

Ping Zhao and Leon P. Van Speybroeck

Harvard-Smithsonian Center for Astrophysics
60 Garden Street, Cambridge, MA 02138 U.S.A.

ABSTRACT

This paper presents a method for modeling the X-ray scattering from random rough surfaces. An actual rough surface is (incompletely) described by its Power Spectral Density (PSD). For a given PSD, model surfaces with the same roughness as the actual surface are constructed by preserving the PSD amplitudes and assigning a random phase to each spectral component. Rays representing the incident wave are reflected from the model surface and projected onto a flat plane, which approximates the model surface, as outgoing rays and corrected for phase delays. The projected outgoing rays are then corrected for wave densities and redistributed onto an uniform grid where the model surface is constructed. The scattering is then calculated by taking the Fast Fourier Transform (FFT) of the resulting distribution. This method is generally applicable and is not limited to small scattering angles. It provides the correct asymmetrical scattering profile for grazing incident radiation. We apply this method to the mirrors of the Chandra X-ray Observatory and show the results. We also expect this method to be useful for other X-ray telescope missions.

Keywords: X-ray scattering, random rough surface, X-ray mirror, X-ray telescope, Chandra X-ray Observatory

1. INTRODUCTION

The study of scattering from random rough surfaces goes back at least to Rayleigh in 1887,[1] and has been investigated by many physicists and engineers. The problem has been the subject of numerous books, including the classic "The Scattering of Electromagnetic Waves From Rough Surfaces" by Beckmann and Spizzichino[2] and countless research papers.[3] Many people have also studied X-ray scattering at grazing angles as part of this subject. This problem is even more difficult because of the short wavelength (compared to the scale of the surface roughness) and the small angle between the wave propagation direction and the surface. Most approaches in the literature make the approximation that the scattering angle is much smaller than the incident grazing angle. Some of the treatments use the approximation that the surfaces are sufficiently "smooth" so that a low order expansion in the surface height errors is adequate, and consequently are limited in their applications. Many of the approaches can not obtain the scattering asymmetry around the direction of specular reflection (scattering towards vs. away from the surface). These approximations are not adequate for many of the applications involving X-ray mirrors.

This new study of the century old problem is motivated by our direct involvement of the evaluation of the X-ray mirror performance aboard the Chandra X-ray Observatory (CXO) – the NASA's third great space observatories now have been successfully operated for three years and have brought us fruitful scientific results with many exciting discoveries. A major achievement of the CXO compared to previous X-ray missions is its unprecedented spatial resolution ($< 0.5''$ FWHM). This is mainly due to the design and manufacture of its X-ray mirrors. These mirrors are the largest, most precise grazing incidence optics ever built. At 0.84-m long and 0.6 – 1.2-m in diameters, the surface area of each mirror ranging from 1.6 to 3.2 square meters. They were polished to the highest quality ever achieved for any X-ray mirrors of this size. The surface roughness of these mirrors is comparable to or less than the X-ray wavelengths in the 0.1–10 keV band over most of the mirror surfaces.

Further author information: Ping Zhao: E-mail: zhao@cfa.harvard.edu

However, the mirrors are not perfect, and consequently there are still small amount of scattered X-rays. We need an accurate model of the X-ray scattering to fully evaluate the CXO performance and analyze the scientific data. We have built a raytrace computer model to simulate the CXO performance. In the current raytrace model, the reflection and scattering are treated as separate effects. Each ray hit the mirror is reflected according the reflectivity of the surface geometry and the low frequency surface map, but not the high frequency roughness, therefore the effect of the surface roughness on the reflection efficiency is lost. The scattering is treated with small (scattering) angle approximation.

Our new method treats the reflection and scattering together, and consequently both depend upon the surface roughness. It does not require the approximation that the scattering angle is small compared to the grazing angle so that all the scattered rays can be traced accurately.

2. POWER SPECTRAL DENSITY OF ROUGH SURFACES

A rough surface is described, statistically, by its surface Power Spectral Density (PSD) as a function of the surface spatial frequency, f. Consider a 1-dimensional surface with length L and surface height (i.e. deviation from a perfectly flat surface): $z = h(x)$, which assumes the value z $(-\infty < z < \infty)$. Its PSD is defined as:*

$$PSD(f) \equiv 2W_1(f) = \frac{2}{L} \left| \int_{-L/2}^{L/2} e^{\imath 2\pi x f} h(x) dx \right|^2 \tag{1}$$

The PSD, as it is defined, is the "spectrum" of the surface roughness. Its value at f is simply the "power" at that frequency. It is easy to distinguish between periodic and random rough surfaces from their PSDs. For periodic rough surfaces, there are some "spectral lines" in their PSDs; while these lines don't exist for a real random rough surface.

Given a PSD function $2W_1$, the surface roughness amplitude RMS in the frequency band of $f_1 - f_2$ (both f_1 and f_2 are positive) can be calculated as:

$$\sigma^2_{f_1 - f_2} = \int_{f_1}^{f_2} 2W_1(f) df \tag{2}$$

3. CHANDRA X-RAY OPTICS

The Chandra X-ray optics – High Resolution Mirror Assembly (HRMA) – is an assembly of four nested Wolter Type-I (paraboloid and hyperboloid) grazing incidence mirrors made of Zerodur and coated with iridium (Ir).[4–6] The mirror elements were polished by Hughes Danbury Optical Systems, Inc. (HDOS) in Danbury, CT. The surface roughness was measured during the HDOS metrology measurements after the final polishing, but before the iridium coating.[7] Tests conducted on sample flats before and after the coating indicate that the coating does not change the surface roughness.

The instruments used for the measurements were the Circularity and Inner Diameter Station (CIDS), the Precision Metrology Station (PMS), and the Micro Phase Measuring Interferometer (MPMI, aka WYKO). The CIDS was used to determine the circularity and the inner diameters. The PMS was used to measure along individual axial meridians. With these two instruments, HDOS essentially measured the 'hoops' and 'staves' of each mirror barrel, and thus mapped the entire surface. The micro-roughness was sampled along meridian at different azimuths using the WYKO instrument at three different magnifications ($\times 1.5$, $\times 10$ & $\times 40$).[7,8]

These metrology data were Fourier transformed and filtered. The low frequency parts of the CIDS and PMS data were used to form mirror surface deformation (from the designed mirror surface) maps. The high frequency parts of the PMS data and the WYKO data were used to estimate the surface micro-roughness. Both of them are parts of the HRMA model we built for the raytrace simulation of the Chandra performance.

*The definition $2W_1$ is conventional, where the subscript $_1$ denotes 1-dimensional; the PSD satisfies $PSD(-f) = PSD(f)$, and typically positive frequency limits are used for most spectral integrals. The total power, σ^2, is the integral of $2W_1$ from $f = 0$ to ∞, i.e. $\sigma^2 = \int_0^\infty 2W_1(f) df$.

Table 1. HRMA Mirror Sections and Their Surface Roughness

HRMA Mirror	Sections Surface Roughness Amplitude RMS $\sigma_{1-1000/\mathrm{mm}}$ (Å)											Num of Sections
P1		LC	LB	LA	M (88%)	SA	SB	SC				7
		50.3	8.49	4.51	3.58	4.91	5.94	53.9				
P3			LB	LA	M (92%)	SA	SB					5
			5.37	5.26	1.96	2.38	4.83					
P4			LB	LA	M (93%)	SA	SB					5
			6.41	3.15	2.57	3.21	6.81					
P6			LB	LA	M (94%)	SA	SB					5
			37.1	5.23	3.34	5.65	20.9					
H1	LD	LC	LB	LA	M (88%)	SA	SB	SC	SD	SE	SF	11
	26.9	5.34	3.64	3.34	3.32	3.32	3.32	3.32	3.53	7.30	60.3	
H3		LC	LB	LA	M (92%)	SA	SB	SC	SD			8
		4.87	2.90	2.23	2.08	2.08	2.10	3.95	5.56			
H4	LD	LC	LB	LA	M (93%)	SA	SB	SC	SD	SE		10
	7.18	3.83	2.61	2.57	2.36	2.36	2.74	2.68	4.01	29.4		
H6	LD	LC	LB	LA	M (94%)	SA	SB	SC	SD	SE		10
	19.0	4.92	2.51	2.23	1.95	1.95	1.95	2.07	2.96	15.9		
Total												61

The mirror surface micro-roughness has little variation with azimuth, but tends to become worse near the mirror ends. We divided the data for each mirror into several axial sections which were selected so that the measured roughness at several places within a section were reasonably uniform; this resulted in a total of 61 sections. We then averaged the PSD measurements within each section to provide an estimate of the PSD for that portion of the mirror element. Table 1 shows the resulting surface roughness in the 61 HRMA mirror sections. The eight mirrors are named P1,3,4,6 (paraboloid) and H1,3,4,6 (hyperboloid) due to historical reasons (there were 6 mirror pairs when the HRMA was designed). The number underneath each section name is the surface roughness amplitude RMS, $\sigma_{1-1000/\mathrm{mm}}$, calculated according to Eq. (2) for $f = 1 - 1000$ mm^{-1}. Each mirror is 838.2 mm in length. The middle sections (M), which are the best polished and hence have the lowest PSDs, cover most part of the mirror surface (the number in parentheses after each M denote the percentage coverage). The σ's for the M sections are only 2–3 Å. The end sections, where the σ's are relatively higher, cover a very small part of the mirror ($< 1\%$), and hence contribute very little to the mirror performance.

Figures 1 and 2 show the PSDs of the M (middle) and SC (small end) sections of P1. P1 and H1 were the first polished mirror pair and are slightly "rougher" than other pairs (see Table 1). The dash and dotted lines show the data from different measurements: the PMS data are in the low frequency range ($f = 0.001 - 0.3$ mm^{-1}); the WYKO data with 3 magnifications are in the higher frequency range ($f = 0.3 - 1000$ mm^{-1}). The solid line is the combined PSD from all four frequency ranges. The SC section obviously is much rougher than the M section.

4. MODEL SURFACES

Typically, a random rough surface is only described by its PSD. Most of the methods calculate the scattering from the surface PSD. However, our method calculates the scattering directly from the surface high frequency spatial profile. Therefore, we first need to construct a model surface that is consistent with a given PSD. From a random rough surface profile, one can derive a unique PSD. But from a given PSD one can't construct the original surface, because the phase information was lost when deriving the PSD. However, one can construct many model surfaces with the same roughness as the original one from the given PSD by assigning different random phase factors to the spectral component.

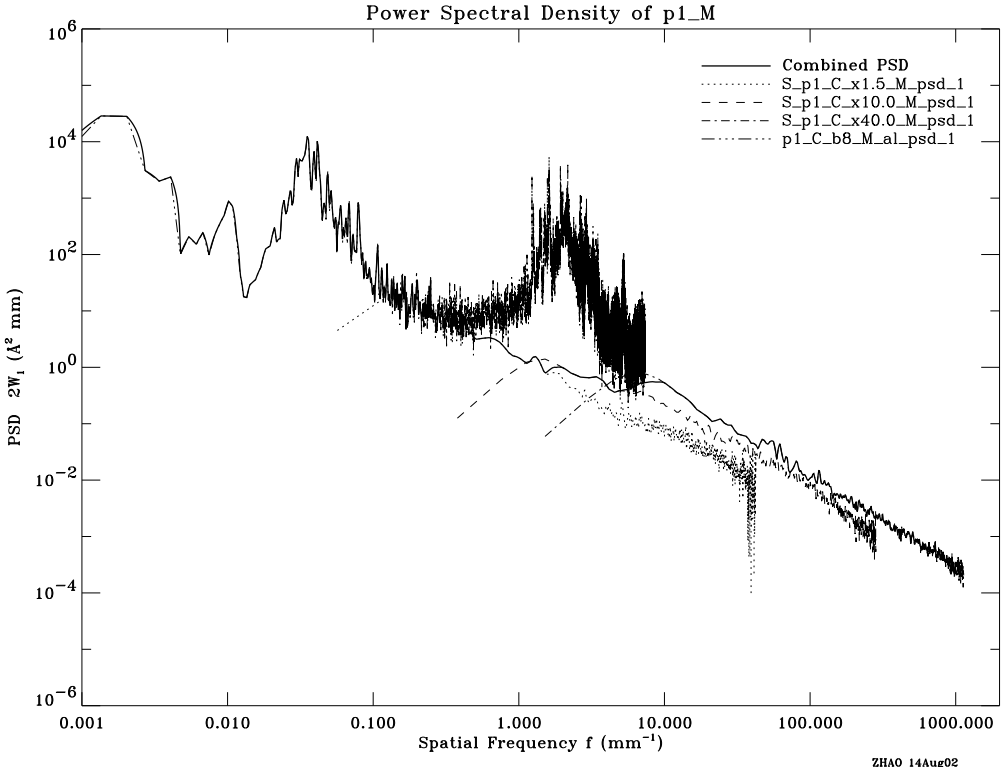

Figure 1. Surface PSD of Chandra mirror P1-M, the middle section of mirror P1.

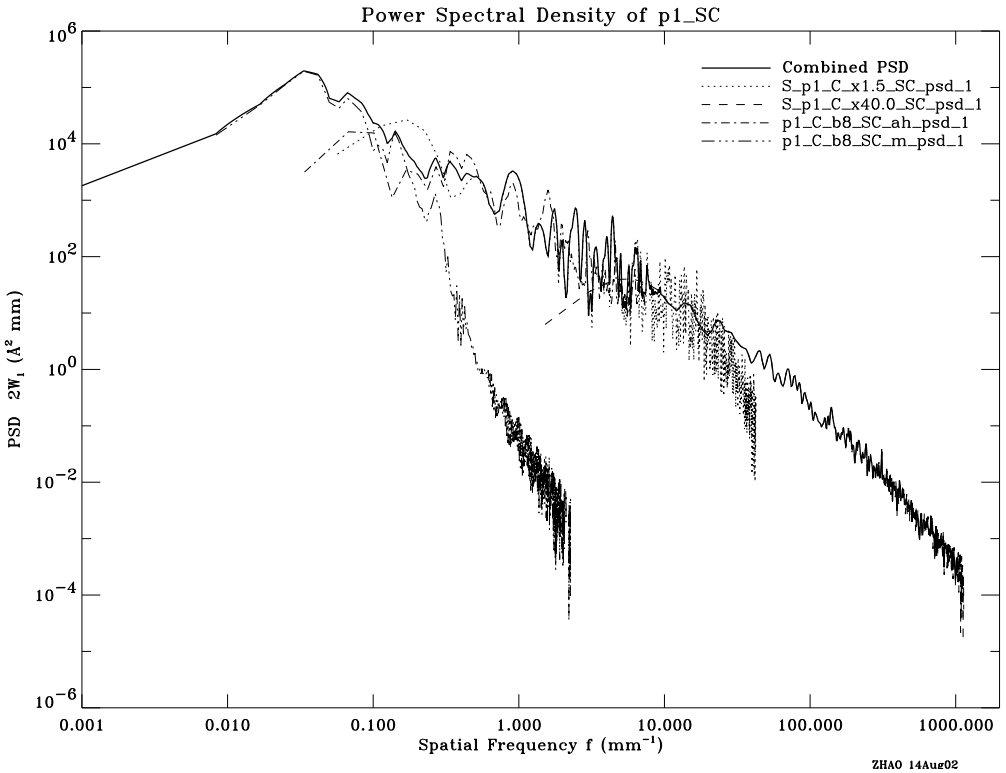

Figure 2. Surface PSD of Chandra mirror P1-SC, the small end section of mirror P1.

To construct a 1-dimensional model surface with length L, we need to obtain N consecutive surface height values $h_i = h(x_i)$ with a fixed interval Δx to cover the surface (i.e. $N\Delta x = L$), and its surface tangent values $h'_i = h'(x_i)$. In Appendix A, we show that h_i and h'_i can be computed from the surface PSD using the following Fourier transforms:

$$h_i = \frac{1}{N} \sum_{j=-(N/2-1)}^{N/2} H_j \; e^{-\imath \frac{2\pi ij}{N}} \tag{3}$$

$$h'_i = \frac{1}{N} \sum_{j=-(N/2-1)}^{N/2} (-\imath 2\pi f_j \; H_j) \; e^{-\imath \frac{2\pi ij}{N}} \tag{4}$$

where $H_j = N\sqrt{\frac{PSD(f_j)\;\Delta f}{2}}\; e^{\imath\varphi_j}$, φ_j is the assigned random phase factor, and $\Delta f = 1/N\Delta x$. Both h_i and h'_i are real, this requires $H_{-j} = H_j^*$, i.e. $PSD(f_{-j}) = PSD(f_j)$ and $\varphi_{-j} = -\varphi_j$.

To construct the model surfaces of HRMA, we choose $N = 2^{21}$ and $\Delta x = 0.0004$ mm. So $L = N\Delta x = 838.86$ mm, and $\Delta f = 1/N\Delta x = 0.001192$ mm^{-1}. Figures 3 and 4 show one set of model surface sections P1-M and P1-SC, constructed using Eqs. (3) and (4) with these parameters.

5. SCATTERING FROM MODEL SURFACES

In this section, we calculate the scattering of plane incident waves from a surface model; most of the detailed derivations of the formulae can be found in Appendices B and C.

We assume that the surfaces are sufficiently smooth so that: 1) there is no shadowing of one part of the surface by another; and 2) there is no reflection from one part of the surface to another, i.e. there are no multiple reflections by the same surface. For an incident plane wave with grazing angle θ_1, the first condition requires that the absolute values of all the surface tangents, $|h'_i|$, are less than θ_1. The second condition requires $|h'_i|$ less than $\theta_1/2$ (when $h'_i = -\theta_1/2$, the reflected wave is parallel to the surface). The first condition is automatically satisfied when the second condition is met. So the surface smoothness condition for applying this method is:

$$|h'_i| < \frac{\theta_1}{2} \tag{5}$$

This condition is easily satisfied for all 61 sections of the HRMA, as can be seen by comparing the tangent distributions in Figures 3 and 4 with the mean grazing angles of the four shells $(51.26', 41.27', 36.43', 27.08')$,

The scattering in the transverse direction, i.e. the off-plane scattering, is smaller than that in the plane of incidence by approximately a factor of the grazing angle, and consequently is less than the uncertainties in our surface PSD. Therefore, in this paper, we ignore the off-plane scattering and limit our discussion to a 1-dimensional surface.

The scattering formula is given by the discrete Fourier transform of the field on the flat surface S_0, as shown in Eq. (58) in Appendix C:

$$I(\theta_{j+q/p}) = \mathcal{A} \left(\frac{\Delta x \; sin(\theta_1 - \theta_{j+q/p})}{\lambda} \right)^2 \left| \sum_{i=-(N/2-1)}^{N/2} \left(\mathbf{E}_i e^{\imath \frac{2\pi iq/p}{N}} \right) \; e^{\imath \frac{2\pi ij}{N}} \right|^2 \qquad (q = 0, 1, \ldots, p-1) \tag{6}$$

where the scattering intensity I is a function of the scattering angle $\theta_{j+q/p}$, which is the deviation from the specular reflection direction towards the surface; λ is the wavelength; $\mathbf{E}_i$ is the field amplitude, after the reflection, on the flat surface at the uniform grid x_i where the model surface was constructed. As described in Appendix C.3, $\mathbf{E}_i$ is a function of the incident wave, the model surface height and tangent, and the local reflectivity. $\mathcal{A}$ is a normalization factor given by Eq. (63). Again we choose $N = 2^{21}$ to use the entire length of the model surface for the FFT computation.

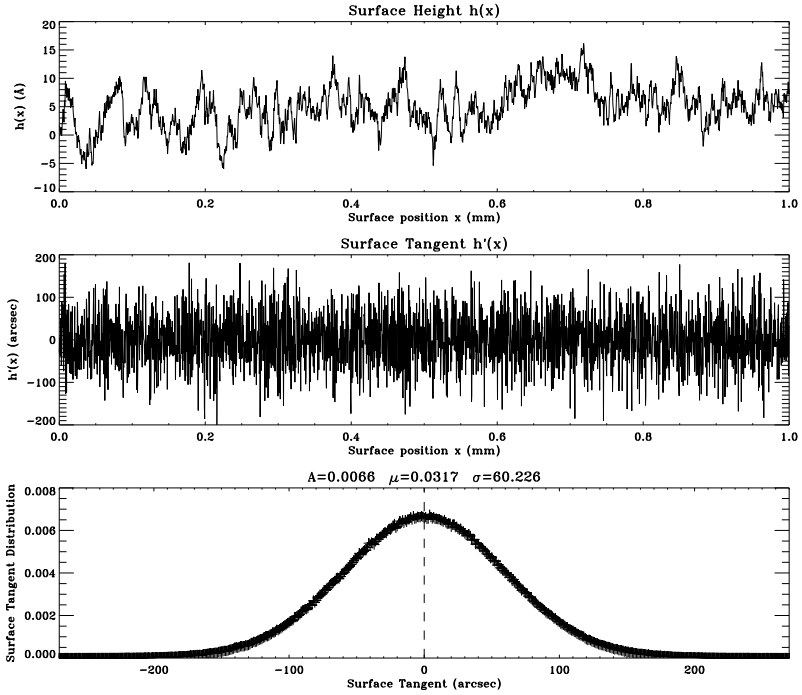

Figure 3. A model surface of Chandra mirror section P1-M, which covers 88% of the mirror P1. The top two panels show the surface height and the surface tangent for a 1 mm section of the model mirror. The bottom panel shows the surface tangent distribution of the entire surface, which can be described accurately by a Gaussian with $\sigma = 60.2''$.

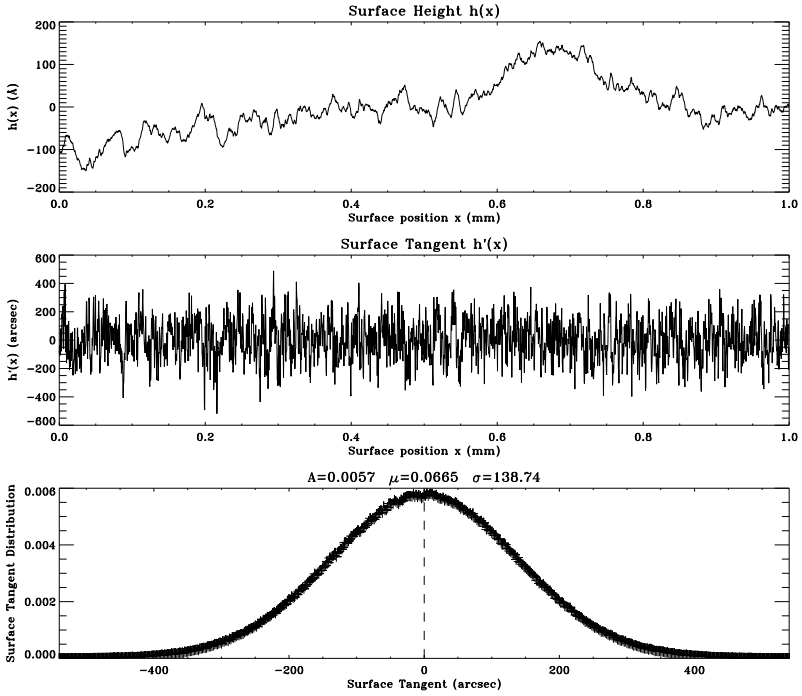

Figure 4. A model surface of Chandra mirror section P1-SC, which is the "worst" end-section of the P1 mirror. The top two panels show the surface height and the surface tangent for a 1 mm section of the model mirror. The bottom panel shows the surface tangent distribution of the entire surface, which can be described accurately by a Gaussian with $\sigma = 138.7''$.

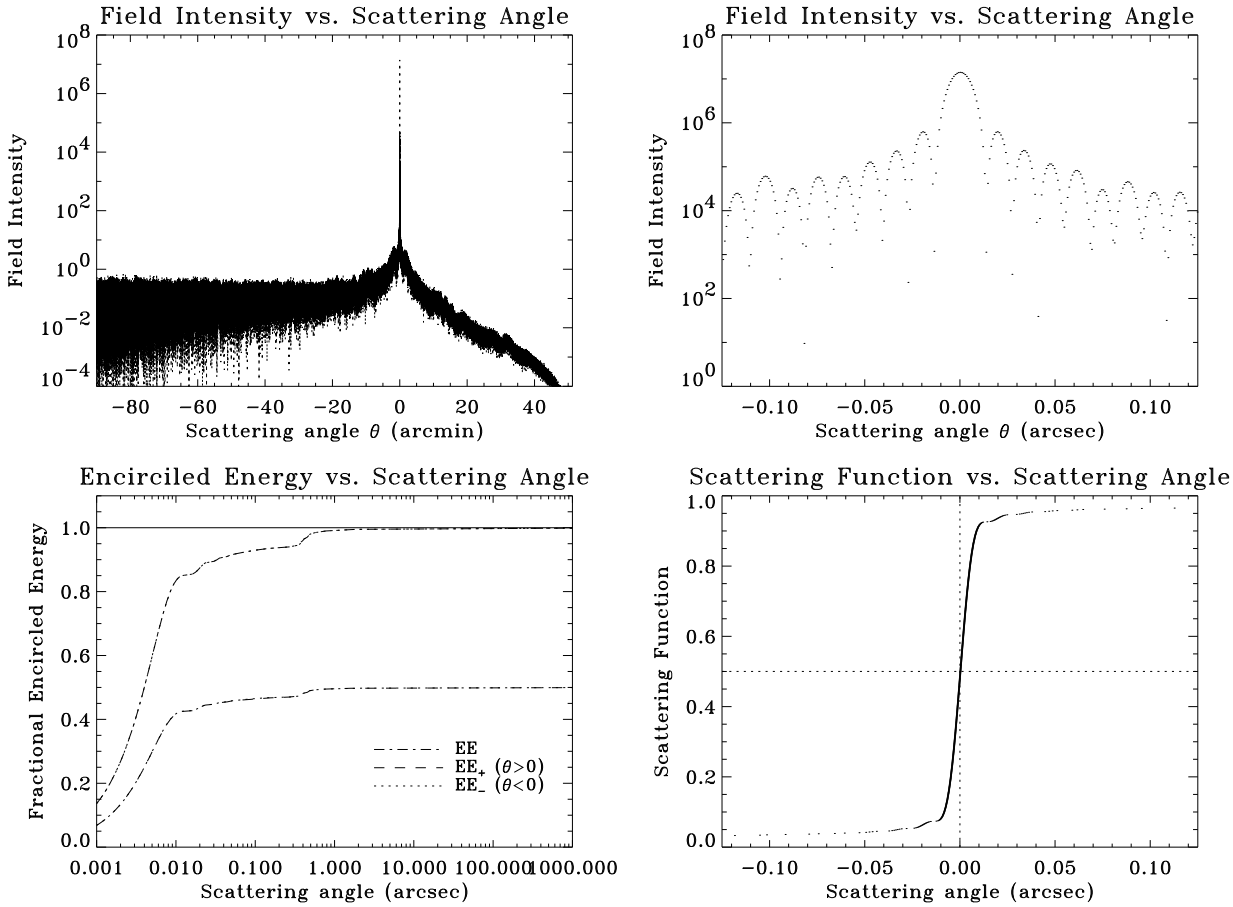

Figure 5. The scattering of 1.49 keV X-rays at $51.26'$ grazing incident angle from the model surface P1-M. The top-left panel shows the scattering field intensity verses the scattering angle. The very sharp peak is at the specular reflection direction $\theta = 0$. The asymmetric nature of the scattering is clearly shown. The top-right panel is the same plot but zoomed into the core of the peak; it shows the Fraunhofer diffraction pattern due to the finite mirror length. The bottom-left panel shows the fractional Encircled Energy (EE) verses the scattering angle, for both sides of the specular direction, and also their sum. The bottom-right panel shows the scattering function $\mathcal{S}$ verses the scattering angle in the same range as the top-right panel.

Figures 5 and 6 show the scattering results for 1.49 keV X-rays incident upon the mirror P1 at its mean grazing angle ($51.26'$). The top two panels show the scattering field intensity verses the scattering angle. The sharp peak of specular reflection (top-left) and the Fraunhofer diffraction pattern (top-right) are shown as expected. The bottom two panels show the fractional Encircled Energies EE_+, EE_-, EE and the scattering function $\mathcal{S}$ defined as:

$$EE_+(\theta) \equiv \frac{1}{\mathcal{E}_s}\int_0^{\theta} I(\theta)\,d\theta = \frac{1}{\mathcal{R}\,\mathcal{E}_i}\int_0^{\theta} I(\theta)\,d\theta \tag{7}$$

$$EE_-(\theta) \equiv \frac{1}{\mathcal{E}_s}\int_{-\theta}^{0} I(\theta)\,d\theta = \frac{1}{\mathcal{R}\,\mathcal{E}_i}\int_{-\theta}^{0} I(\theta)\,d\theta \tag{8}$$

$$EE(\theta) \equiv \frac{1}{\mathcal{E}_s}\int_{-\theta}^{\theta} I(\theta)\,d\theta = \frac{1}{\mathcal{R}\,\mathcal{E}_i}\int_{-\theta}^{\theta} I(\theta)\,d\theta \tag{9}$$

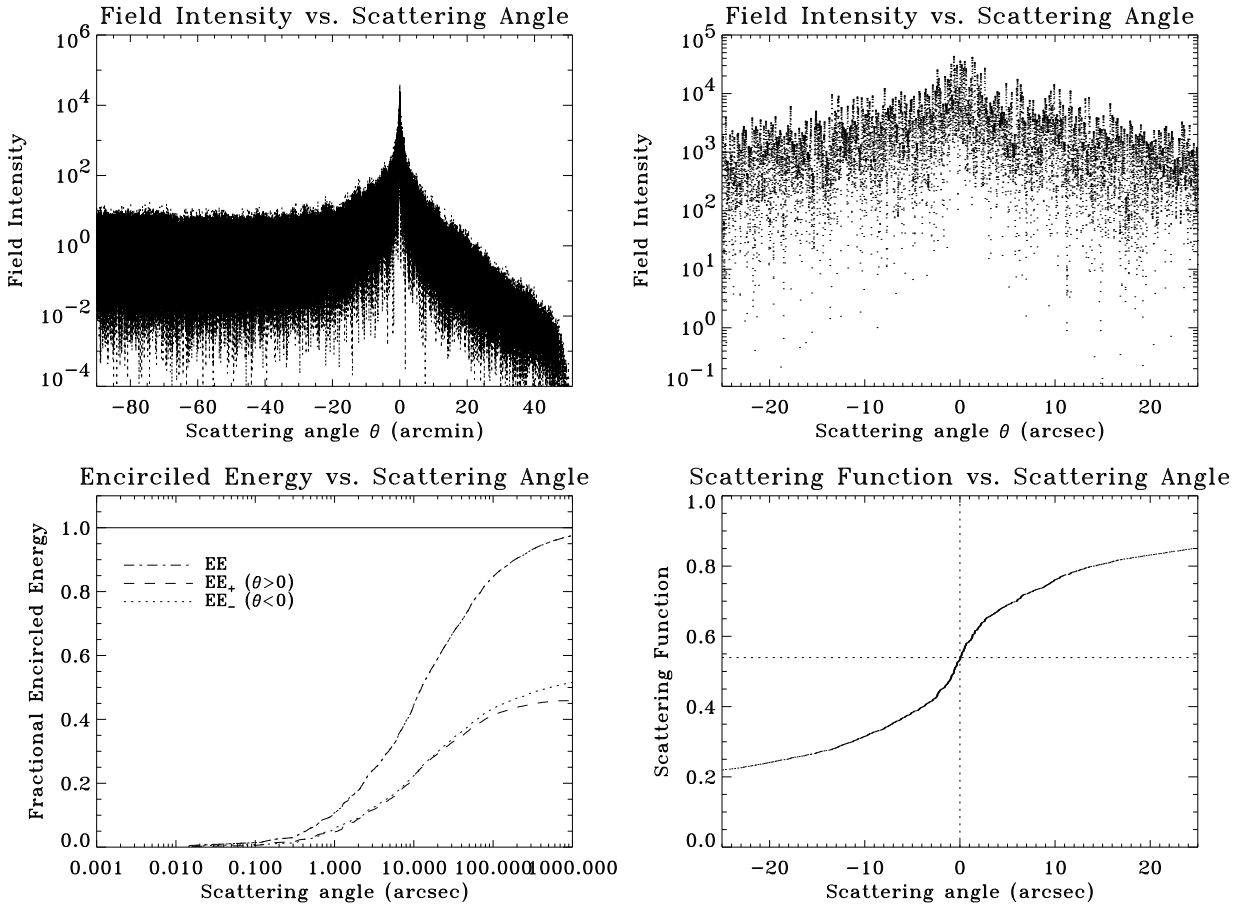

Figure 6. Scattering from model surface P1-SC. It has much broader scattering peak than P1-M.

$$\mathcal{S}(\theta) \equiv \frac{1}{\mathcal{E}_s}\int_{-\infty}^{\theta} I(\theta)\,d\theta = \frac{1}{\mathcal{R}\,\mathcal{E}_i}\int_{-\infty}^{\theta} I(\theta)\,d\theta \tag{10}$$

where $\mathcal{E}_i$, $\mathcal{E}_s$ and $\mathcal{R}$ are the total incident and scattered energy, and the reflectivity of the rough surface as described in Appendix C.5.

6. SUMMARY AND FUTURE WORK

We have developed a method to model the wave scattering from random rough surfaces. Model surfaces with the same roughness as the actual surface are constructed from the actual PSD. The scattering from the model surfaces is calculated using the scattering formulae we derived in this paper. These scattering formulae are based on the general Kirchhoff equations but without small angle approximations. This method treats the reflection and scattering together and provides the dependence of the reflectivity on the surface roughness. It is applicable in general and is especially useful for X-ray scattering at grazing angles. We have applied this method to the mirrors of the Chandra X-ray Observatory and have shown that the calculated scattering profile is as expected, including the Fraunhofer scattering patterns which result from the finite length of the surfaces.

This work is still continuing. Next we will generate scattering tables, which are the tabulations of the scattering function $\mathcal{S}$. Then we will use these scattering tables in our raytrace model to simulate the CXO performance and compare it with the real results of the CXO, from both on-orbit observations and its ground calibrations. This method should be useful for other X-ray telescope missions as well.

APPENDIX A. CONSTRUCTION OF MODEL SURFACES

A.1. Fourier Transform

The **Continuous Fourier Transform** equations are[9]:

$$H(f) = \int_{-\infty}^{\infty} h(x)\ e^{\imath 2\pi x f}\ dx \qquad (forward) \tag{11}$$

$$h(x) = \int_{-\infty}^{\infty} H(f)\ e^{-\imath 2\pi x f}\ df \qquad (inverse) \tag{12}$$

Here if h is a function of position, x, in mm, H will be a function of spatial frequency, f, in mm^{-1}.

When there are N consecutive sampled values at $x = x_i$ with the sampling interval Δx, we make the transform:

$$x \Rightarrow x_i \equiv i\ \Delta x, \qquad h(x) \Rightarrow h_i \equiv h(x_i), \qquad i = -(\frac{N}{2} - 1), \ldots, -1, 0, 1, \ldots, \frac{N}{2} \tag{13}$$

$$f \Rightarrow f_j \equiv j\ \Delta f, \qquad H(f) \Rightarrow H_j \equiv \frac{H(f_j)}{\Delta x}, \quad j = -(\frac{N}{2} - 1), \ldots, -1, 0, 1, \ldots, \frac{N}{2} \tag{14}$$

where $\Delta x \Delta f = 1/N$. We obtain the **Discrete Fourier Transform** equations:

$$H_j = \sum_{i=-(N/2-1)}^{N/2} h_i\ e^{\imath \frac{2\pi i j}{N}} \qquad (forward) \tag{15}$$

$$h_i = \frac{1}{N} \sum_{j=-(N/2-1)}^{N/2} H_j\ e^{-\imath \frac{2\pi i j}{N}} \qquad (inverse) \tag{16}$$

A.2. Surface Height

From Eq (1), we obtain:

$$PSD(f) = \frac{2}{L} \left| \int_{-L/2}^{L/2} e^{\imath 2\pi x f} h(x) dx \right|^2 \quad \Longrightarrow \quad \sqrt{\frac{PSD(f)\ L}{2}} = \left| \int_{-L/2}^{L/2} e^{\imath 2\pi x f} h(x) dx \right| \tag{17}$$

Here $PSD(f)$ is a real continuous function of the spatial frequency f. We first need to convert Eq (17) to a discrete Fourier transform. Using the equations in A.1 and relation $L = N\Delta x = 1/\Delta f$, we obtain:

$$|H_j| = \frac{|H(f_j)|}{\Delta x} = \frac{1}{\Delta x}\sqrt{\frac{PSD(f_j)\ L}{2}} = N\sqrt{\frac{PSD(f_j)\ \Delta f}{2}} = \left| \sum_{i=-(N/2-1)}^{N/2} h_i\ e^{\imath \frac{2\pi i j}{N}} \right| \tag{18}$$

Therefore H_j can be expressed as the forward Fourier transform of h_i as

$$H_j = N\sqrt{\frac{PSD(f_j)\ \Delta f}{2}} e^{\imath \varphi_j} = \sum_{i=-(N/2-1)}^{N/2} h_i\ e^{\imath \frac{2\pi i j}{N}} \tag{19}$$

Hence the surface height, $h(x_i) = h_i$, can be expressed as the inverse Fourier transform of H_j

$$h_i = \frac{1}{N} \sum_{j=-(N/2-1)}^{N/2} H_j\ e^{-\imath \frac{2\pi i j}{N}} = \frac{1}{N} \sum_{j=-(N/2-1)}^{N/2} N\sqrt{\frac{PSD(f_j)\ \Delta f}{2}} e^{\imath \varphi_j}\ e^{-\imath \frac{2\pi i j}{N}} \tag{20}$$

where φ_j is a random phase factor. A set of surface heights, h_i, can be generated from a set of phase factor φ_j. Therefore for a given PSD, we can generate as many sets of surface map (of the same roughness) as we want by changing the random phase factor φ_j. Because h_i, the surface height, has to be real, this requires $H_{-j} = H_j^*$, i.e. $PSD(f_{-j}) = PSD(f_j)$ and $\varphi_{-j} = -\varphi_j$.

A.3. Surface Tangent

Since

$$h_i \;=\; \frac{1}{N} \sum_{j=-(N/2-1)}^{N/2} H_j \; e^{-\imath \frac{2\pi ij}{N}} \;=\; \frac{1}{N} \sum_{j=-(N/2-1)}^{N/2} H_j \; e^{-\imath 2\pi x_i f_j} \tag{21}$$

The surface tangent can be obtained by taking the derivative on both sides of Eq. (21) with respect to x_i:

$$h'_i \;=\; \frac{1}{N} \sum_{j=-(N/2-1)}^{N/2} (-\imath 2\pi f_j \; H_j) \; e^{-\imath 2\pi x_i f_j} \;=\; \frac{1}{N} \sum_{j=-(N/2-1)}^{N/2} (-\imath 2\pi f_j \; H_j) \; e^{-\imath \frac{2\pi ij}{N}} \tag{22}$$

The surface tangent h'_i also has to be real. This condition is automatically satisfied because

$$-\imath 2\pi f_{-j} \; H_{-j} \;=\; -\imath 2\pi (-f_j) \; H_j^* \;=\; \imath 2\pi f_j \; H_j^* \;=\; (-\imath 2\pi f_j \; H_j)^* \tag{23}$$

APPENDIX B. KIRCHHOFF SOLUTION

The wave scattering from random rough surfaces is described by the Kirchhoff solution[2] and its far-field approximation.

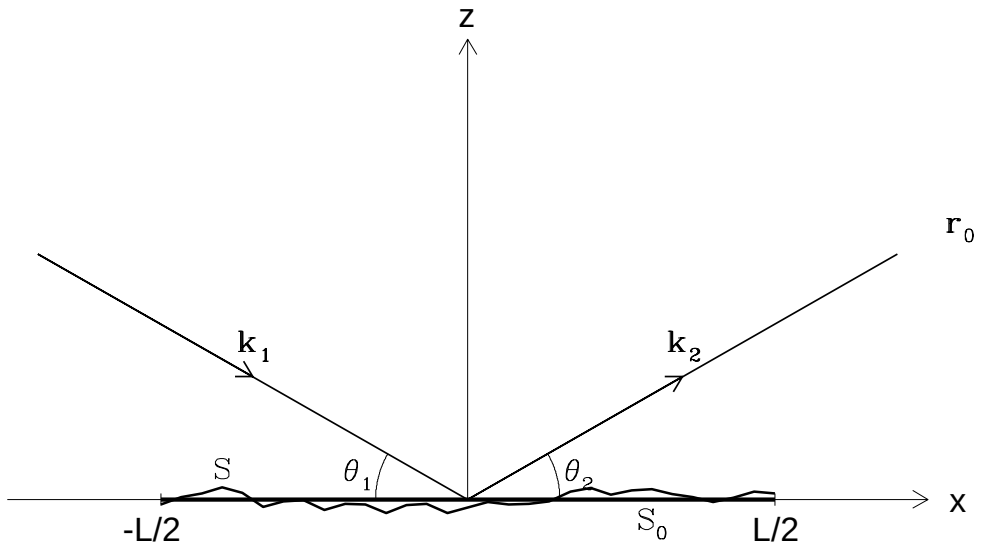

Figure 7. Wave scattering from a random rough surface. A flat surface S_0 with $z = 0$ lies in the **x-y** plane (**y**-axis not shown). A rough surface S has surface height $z = h(x, y)$, deviates from S_0. The **z** axis is normal to the **x-y** plane and points up. Incident and reflecting (or scattering) wave-vectors are shown as $\mathbf{k}_1$ and $\mathbf{k}_2$. Incident and reflecting grazing angles with respect to the surface S_0 are θ_1 and θ_2. $\mathbf{r}_0$ is the observation point where the scattering is to be measured.

As shown in Figure 7, define:

- S_0 — 2-dimensional flat surface at $z = 0$.
- S — 2-dimensional rough surface, described by its surface height $z = h(x, y)$.
- $\mathbf{E}_1 e^{\imath \mathbf{k_1} \cdot \mathbf{r}} \;=\; \mathbf{E}_1 e^{\imath (k_1 x + k_3 z)}$ — incident plane wave (in the incident plane, therefore $k_2 = 0$).
- $\mathbf{E}_2 e^{\imath \mathbf{k_2} \cdot \mathbf{r}} \;=\; \mathbf{E}_2 e^{\imath (k_x x + k_y y + k_z z)}$ — reflected or scattered wave from the rough surface S.
- θ_1, θ_2 — incident and reflecting grazing angles with respect to the surface S_0.

where $\mathbf{k}_1$ and $\mathbf{k}_2$ are the wave vectors of the incident and scattered waves, so $\mathbf{E}_1 \cdot \mathbf{k}_1 = 0,\ \mathbf{E}_2 \cdot \mathbf{k}_2 = 0$, and

$$k \equiv \frac{2\pi}{\lambda} = |\mathbf{k}_1| = \sqrt{k_1^2 + k_3^2} = |\mathbf{k}_2| = \sqrt{k_x^2 + k_y^2 + k_z^2} \tag{24}$$

A vector normal to the local surface on S is given by:

$$\mathbf{n} = -\nabla(h(x,y) - z) = -\frac{\partial h(x,y)}{\partial x}\hat{\mathbf{x}} - \frac{\partial h(x,y)}{\partial y}\hat{\mathbf{y}} + \hat{\mathbf{z}} \tag{25}$$

The field at an observation point $\mathbf{r}_0$ is given by the integration of contributions from the field $\mathbf{E}(s)e^{\imath(k_1 x + k_3 z)}$ on the surface S:

$$\mathbf{E}(\mathbf{r}_0) = \frac{1}{\imath\lambda}\int_S\int ds\, \mathbf{E}(s)e^{\imath(k_1 x + k_3 z)}\,\frac{e^{\imath kr}}{r^2}\,(\hat{\mathbf{n}}\cdot\mathbf{r}) = \frac{1}{\imath\lambda}\iint dxdy\, \mathbf{E}(s)e^{\imath(k_1 x + k_3 h(x,y))}\,\frac{e^{\imath kr}}{r^2}\,(\mathbf{n}\cdot\mathbf{r}) \tag{26}$$

where ds is an element of surface area; $\mathbf{E}$(s) is given by the incident wave $\mathbf{E}_1$ multiplied by the suitable reflection coefficient; the vector $\mathbf{r}$ goes *from* the point of integration (x, y, z) *to* the observation point (x_0, y_0, z_0), and $r = |\mathbf{r}|$; $\hat{\mathbf{n}}$ is a unit vector in the direction of $\mathbf{n}$, and $(\hat{\mathbf{n}}\cdot\mathbf{r})\,ds = (\mathbf{n}\cdot\mathbf{r})\,dxdy$. Eq. (26) is known as the general Kirchhoff solution for the wave scattering.

Next we derive the far-field approximation of this solution. When the reflecting surface is near the origin of the coordinate system and the observation point is far from the origin, i.e. when ($x \ll x_0$, $y \ll y_0$, $z \ll z_0$), we have:

$$\mathbf{k}_2 = k_x\hat{\mathbf{x}} + k_y\hat{\mathbf{y}} + k_z\hat{\mathbf{z}} = k\frac{(x_0 - x)}{|\mathbf{r}|}\hat{\mathbf{x}} + k\frac{(y_0 - y)}{|\mathbf{r}|}\hat{\mathbf{y}} + k\frac{(z_0 - z)}{|\mathbf{r}|}\hat{\mathbf{z}} \approx \frac{k}{r_0}(x_0\hat{\mathbf{x}} + y_0\hat{\mathbf{y}} + z_0\hat{\mathbf{z}}) \tag{27}$$

$$\mathbf{r} = (x_0 - x)\hat{\mathbf{x}} + (y_0 - y)\hat{\mathbf{y}} + (z_0 - z)\hat{\mathbf{z}} \approx x_0\hat{\mathbf{x}} + y_0\hat{\mathbf{y}} + z_0\hat{\mathbf{z}} \approx \frac{r_0}{k}\,(k_x\hat{\mathbf{x}} + k_y\hat{\mathbf{y}} + k_z\hat{\mathbf{z}}) \tag{28}$$

$$r = |\mathbf{r}| = \sqrt{(x_0 - x)^2 + (y_0 - y)^2 + (z_0 - z)^2} \approx r_0 - \frac{x_0}{r_0}x - \frac{y_0}{r_0}y - \frac{z_0}{r_0}z \tag{29}$$

where $r_0 = |\mathbf{r}_0| = \sqrt{x_0^2 + y_0^2 + z_0^2}$. Keep the first order of r in the phase factor and zeroth order elsewhere:

$$\mathbf{n}\cdot\mathbf{r} \approx -\frac{r_0}{k}\left[k_x\frac{\partial h(x,y)}{\partial x} + k_y\frac{\partial h(x,y)}{\partial y} - k_z\right] \tag{30}$$

$$e^{\imath kr} \approx e^{\imath k(r_0 - \frac{x_0}{r_0}x - \frac{y_0}{r_0}y - \frac{z_0}{r_0}z)} \approx e^{\imath kr_0}\,e^{-\imath(k_x x + k_y y + k_z h(x,y))} \tag{31}$$

Eq. (26) becomes:

$$\mathbf{E}(\mathbf{r}_0) \approx -\frac{1}{\imath\lambda}\iint dxdy\, \mathbf{E}(s)e^{\imath(k_1 x + k_3 z)}\frac{e^{\imath kr_0}}{r_0^2}e^{-\imath(k_x x + k_y y + k_z z)}\frac{r_0}{k}\left[k_x\frac{\partial h(x,y)}{\partial x} + k_y\frac{\partial h(x,y)}{\partial y} - k_z\right] \tag{32}$$

$$= \frac{\imath e^{\imath kr_0}}{2\pi r_0}\iint dxdy\, \mathbf{E}(s)\ e^{\imath(k_1 x + k_3 h(x,y))}\ e^{-\imath(k_x x + k_y y + k_z h(x,y))}\left[k_x\frac{\partial h(x,y)}{\partial x} + k_y\frac{\partial h(x,y)}{\partial y} - k_z\right] \tag{33}$$

$$= \frac{\imath e^{\imath kr_0}}{2\pi r_0}\iint dxdy\, \mathbf{E}(s)e^{\imath[(k_1 - k_x)x - k_y y + (k_3 - k_z)h(x,y)]}\left[k_x\frac{\partial h(x,y)}{\partial x} + k_y\frac{\partial h(x,y)}{\partial y} - k_z\right] \tag{34}$$

This is the far-field approximation of the Kirchhoff solution for the wave scattering.

APPENDIX C. SCATTERING FORMULA

In this section, we derive the scattering formula from the Kirchhoff solution for the constructed model surfaces.

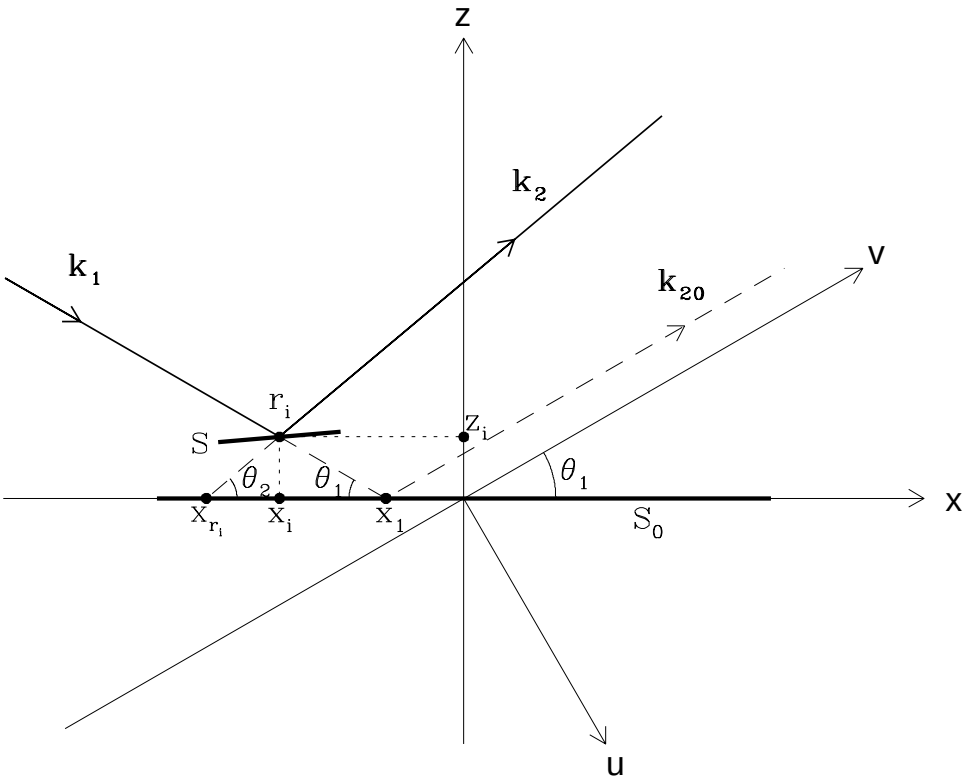

Figure 8. The scattering geometry. The flat surface S_0 is located on the **x** axis. The **z** axis is normal to the surface S_0. The **u-v** axes form a coordinate system that is rotated clockwise from the **x-z** axes by $(\frac{\pi}{2} - \theta_1)$, so the **v** axis is aligned with the specular reflection direction. An incident ray, $\mathbf{k}_1$, comes in from the left with a grazing angle θ_1; had it struck the surface S_0 at x_1, it would have been reflected parallel to the **v** axis as $\mathbf{k}_{20}$. However, it actually strikes the rough surface S at $r_i(x_i, z_i)$, and is reflected at an angle θ_2 as $\mathbf{k}_2$. The intersection of $\mathbf{k}_2$ with the surface S_0 is at x_{r_i}.

C.1. Integral on 1-dimensional flat surface S_0

We first reduce the Kirchhoff solution to a 1-dimensional integral on flat surface S_0. Consider:

- In plane scattering: $k_y = 0$
- One dimensional surface, i.e. $h(x, y)$ only depends on x: $h(x, y) = h(x)$

Eq. (33) becomes:

$$\mathbf{E}(\mathbf{r}_0) \;=\; \frac{\imath e^{\imath k r_0}}{2\pi} \int dx\, \mathbf{E}(s)\; e^{\imath(k_1 x + k_3 h(x))}\; e^{-\imath(k_x x + k_z h(x))} \left[k_x \frac{\partial h(x)}{\partial x} - k_z \right] \tag{35}$$

here we have omitted a dimensionless factor $a = Y/r_0$, where Y is the transverse surface dimension; this factor will be absorbed later in an overall normalization factor $\mathcal{A}$.

Figure 8 shows the scattering geometry. The incident ray, $\mathbf{k}_1$, strikes the rough surface at $r_i(x_i, z_i)$ and is reflected as $\mathbf{k}_2$, where x_i is one of the N positions of the constructed model surface (see Appendix A) and $z_i = h(x_i) = h_i$. The reflected field at r_i is

$$\mathbf{E}(r_i)\, e^{\imath(k_1 x_i + k_3 z_i)} \;=\; \mathbf{E}(x_i, h_i)\, e^{\imath(k_1 x_i + k_3 h_i)} \tag{36}$$

For the integral (35), this is equivalent to have a field at $(x_{r_i}, 0)$, the intersection of $\mathbf{k}_2$ and $\mathbf{x}$ axis, on the surface S_0 described by:

$$\mathbf{E}(x_{r_i}, 0) \;=\; \mathbf{E}(r_i)\, e^{\imath(k_1 x_i + k_3 h_i - k h_i / sin\,\theta_2)} \tag{37}$$

where $kh_i/sin\,\theta_2$ is the phase delay between (x_i, h_i) and $(x_{r_i}, 0)$. Let:

$$\mathbf{E}(x_{r_i}) \;=\; \mathbf{E}(x_{r_i}, 0)\, e^{-\imath k_1 x_{r_i}} \;=\; \mathbf{E}(r_i)\, e^{\imath(k_1 x_i + k_3 h_i - k h_i / sin\,\theta_2 - k_1 x_{r_i})} \;=\; \mathbf{E}(r_i)\, e^{\imath\,\phi_i} \tag{38}$$

So the integral (35) can be written as

$$\mathbf{E}(\mathbf{r}_0) \;=\; \frac{\imath e^{\imath k r_0}}{2\pi} \int dx\, \mathbf{E}(x)\; e^{\imath(k_1 x - k_x x - k_z h(x))} \left[k_x \frac{\partial h(x)}{\partial x} - k_z \right] \tag{39}$$

Now the integration boundary has changed from $\mathbf{E}(s)$ on the rough surface S to $\mathbf{E}(x)$ on the flat surface S_0, so $h(x) = 0$ and $\frac{\partial h(x)}{\partial x} = 0$. Therefore Eq. (39) becomes:

$$\mathbf{E}(\mathbf{r}_0) \;=\; \mathbf{E}(k_x, k_z) \;=\; \frac{\imath e^{\imath k r_0}}{2\pi} \int dx\, \mathbf{E}(x)\; e^{\imath(k_1 - k_x)x}\; (-k_z) \;=\; -\frac{\imath k_z e^{\imath k r_0}}{2\pi} \int dx\, \mathbf{E}(x)\; e^{\imath(k_1 - k_x)x} \tag{40}$$

here the reflected field $\mathbf{E}(x)$ are calculated at non-uniformly distributed, discrete points $x = x_{r_i}$. The position, x_{r_i}, and the phase, ϕ_i, of the field $\mathbf{E}(x_{r_i})$ are:

$$x_{r_i} \;=\; x_i - \frac{h_i}{tan\,\theta_2} \tag{41}$$

$$\begin{aligned} \phi_i \;&=\; k_1 x_i + k_3 h_i - \frac{k h_i}{sin\,\theta_2} - k_1 x_{r_i} \;=\; k \left(cos\,\theta_1 x_i - sin\,\theta_1 h_i - \frac{h_i}{sin\,\theta_2} - cos\,\theta_1 \left(x_i - \frac{h_i}{tan\,\theta_2} \right) \right) \\ &=\; -k h_i \left(sin\,\theta_1 + \frac{1}{sin\,\theta_2} - \frac{cos\,\theta_1}{tan\,\theta_2} \right) \;=\; -\,k\,h_i\, \frac{1 - cos(\theta_1 + \theta_2)}{sin\,\theta_2} \;=\; -\,2\,k\,h_i\, \frac{sin^2 \frac{\theta_1 + \theta_2}{2}}{sin\,\theta_2} \end{aligned} \tag{42}$$

where $k_3 = -k sin\,\theta_1$, because, by definition, the $\mathbf{z}$ axis points up.

Thus for the field $\mathbf{E}(s)$ of each ray $\mathbf{k}_1$ at r_i, we can use its equivalent field $\mathbf{E}(x)$ at x_{r_i} to do the integral ($x_{r_i} < x_i$ when $h_i > 0$, $x_{r_i} > x_i$ when $h_i < 0$).

C.2. Fourier transform with variable ξ

Define a coordinate system **u-v** that is rotated clockwise from the **x-z** axes by $(\frac{\pi}{2} - \theta_1)$, so the $\mathbf{v}$ axis is aligned with the specular reflection direction (see Figure 8). Define the scattering angle, θ, as the angle of deviation clockwise from the $\mathbf{v}$ axis, i.e. $\theta = \theta_1 - \theta_2$. Also define the variable $\xi = \frac{k_1 - k_x}{2\pi}$. Therefore:

$$k_1 \;=\; k\, cos\,\theta_1, \quad k_x \;=\; k\, cos\,\theta_2 \;=\; k\, cos(\theta_1 - \theta), \quad k_z \;=\; k\, sin\,\theta_2 \;=\; k\, sin(\theta_1 - \theta) \tag{43}$$

$$2\pi\xi \;=\; k_1 - k_x \;=\; k\, cos\,\theta_1 - k\, cos(\theta_1 - \theta) \;=\; -\,2\, k\, sin(\theta_1 - \frac{\theta}{2})\, sin\,\frac{\theta}{2} \tag{44}$$

$$\theta \;=\; \theta_1 - cos^{-1} \left(cos\,\theta_1 - \frac{2\pi\xi}{k} \right) \;=\; \theta_1 - cos^{-1} (cos\,\theta_1 - \xi\lambda) \tag{45}$$

The scattering equation (40) becomes:

$$\mathbf{E}(\mathbf{r}_0) \;=\; \mathbf{E}(\xi(\theta)) \;=\; -\,\frac{\imath e^{\imath k r_0} k\; sin(\theta_1 - \theta)}{2\pi} \int dx\, \mathbf{E}(x)\, e^{\imath 2\pi\xi x} \;=\; -\,\frac{\imath e^{\imath k r_0} sin(\theta_1 - \theta)}{\lambda} \int dx\, \mathbf{E}(x)\, e^{\imath 2\pi\xi x} \tag{46}$$

Thus, the scattering field $\mathbf{E}(\xi)$ can be obtained from the Fourier transform integral of the field $\mathbf{E}(x)$ on the surface S_0. And it can be can be expressed as $\mathbf{E}(\theta)$ using Eq. (44).

C.3. Discrete Fourier transform at x_i

In practice, this integral is performed numerically using the Fast Fourier Transform (FFT) on N uniformly distributed points x_i's where we constructed the model surface. Therefore we need to convert the field $\mathbf{E}(x_{r_i})$ to the field $\mathbf{E}(x_i)$. This can be simply done by multiplying $\mathbf{E}(x_{r_i})$ with two factors:

$$\mathbf{E}(x_i) \;=\; A_i\, B_i\, \mathbf{E}(x_{r_i}) \;=\; A_i\, B_i\, \mathbf{E}(x_i - \frac{h_i}{tan\,\theta_2}) \;=\; A_i\, B_i\, \mathbf{E}(r_i)\, e^{\imath\phi_i} \tag{47}$$

Where the factor A_i is used to adjust the incident plane wave density due to the different surface height h_i's at the uniform grid x_i's; it is calculated by intercepting all the incident rays that strike on the surface S at (x_i, h_i)'s with a coordinate that is perpendicular to the direction of incidence. Let the intercepting points be w_i's on the coordinate. Then:

$$A_i \;=\; \frac{w_{i+1} - w_{i-1}}{2\,\Delta x\, sin\theta_1} \tag{48}$$

The factor B_i is used to adjust the outgoing ray density due to the redistribution of the reflected rays from the non-uniform grid x_{r_i} to the uniform grid x_i. For example, when the point x_{r_i} falls between the fixed grid points x_{i-1} and x_i $(x_i - x_{i-1} = \Delta x)$, then

$$\frac{x_i - x_{r_i}}{\Delta x}\, \mathbf{E}(x_{r_i}) \quad \text{is added to field} \quad \mathbf{E}(x_{i-1}) \tag{49}$$

$$\frac{x_{r_i} - x_{i-1}}{\Delta x}\, \mathbf{E}(x_{r_i}) \quad \text{is added to field} \quad \mathbf{E}(x_i) \tag{50}$$

This process is done for each ray until all the fields are redistributed to the uniform grid x_i.

Having obtained the field $\mathbf{E}(x_i)$ on uniform grid, x_i, we can rewrite the scattering equation (46) as the discrete Fourier transform (see Appendix A.1). Let:

$$x \;\Rightarrow\; x_i \equiv i\;\Delta x, \qquad \mathbf{E}(x) \;\Rightarrow\; \mathbf{E}_i \equiv \mathbf{E}(x_i), \qquad i = -(\frac{N}{2} - 1), \ldots, -1, 0, 1, \ldots, \frac{N}{2} \tag{51}$$

$$\xi \;\Rightarrow\; \xi_j \equiv j\;\Delta\xi, \qquad \mathbf{E}(\xi) \;\Rightarrow\; \mathbf{E}_j \equiv \frac{\mathbf{E}(\xi_j)}{\Delta x}, \qquad j = -(\frac{N}{2} - 1), \ldots, -1, 0, 1, \ldots, \frac{N}{2} \tag{52}$$

where $\Delta x \Delta\xi = 1/N$. The scattering equation (46) becomes:

$$\mathbf{E}_j \;\equiv\; \frac{\mathbf{E}(\xi_j)}{\Delta x} \;=\; -\,\frac{\imath e^{\imath k r_0} sin(\theta_1 - \theta_j)}{\lambda} \sum_{i=-(N/2-1)}^{N/2} \mathbf{E}_i\; e^{\imath\frac{2\pi ij}{N}} \tag{53}$$

where

$$\mathbf{E}_i \;=\; \mathbf{E}(x_i) \;=\; A_i\, B_i\, \mathbf{E}(r_i)\, e^{\imath\phi_i} \;=\; A_i\, B_i\, \mathbf{E}_1\, R(\theta_1 + tan^{-1}(h_i'))\, e^{\imath\phi_i} \tag{54}$$

where $R(\theta_1 + tan^{-1}(h_i'))$ is the reflection coefficient of ray i with the local grazing angle, $\theta_1 + tan^{-1}(h_i')$, on the rough surface S. h_i' is the local surface tangent of the model surface.

The scattering intensity, I, is given as a function of the scattering angle, θ, by:

$$I(\theta_j) \;=\; I(\xi(\theta_j)) \;\equiv\; \mathcal{A}\,\mathbf{E}(\xi_j)\,\mathbf{E}^*(\xi_j) \;=\; \mathcal{A}\left(\frac{\Delta x\, sin(\theta_1 - \theta_j)}{\lambda}\right)^2 \left|\sum_{i=-(N/2-1)}^{N/2} \mathbf{E}_i\; e^{\imath\frac{2\pi ij}{N}}\right|^2 \tag{55}$$

where $\mathcal{A}$ is a normalization factor which we will derive in section C.5.

C.4. Scattering formula – the Fraunhofer diffraction pattern

With the Eq. (55), it seems that we can finally obtain the profile of scattering from the rough surface. However, this is not quite true, because of the discrete Fourier transform. The main disadvantage of the discrete Fourier transform is (what else?) "discrete". Its shortcomings are displayed perfectly in this case. Eq. (55) is correct, but all of the points except the central peak ($\theta_j = 0$) are calculated in the valleys of the Fraunhofer diffraction pattern at:

$$\theta_j \;=\; -\frac{j\;\lambda}{N\,\Delta x\,sin\,\theta_1} \;=\; -\frac{j\;\lambda}{L\,sin\,\theta_1}, \qquad j = \pm 1, \pm 2, \pm 3, \ldots \tag{56}$$

where L is the surface length. In case of a perfect surface, Eq. (55) gives $I(\theta_j) = 0$ except for one point at $j = 0$, and the correct diffraction pattern from the finite surface length is not obtained. To get the diffraction patterns at angles between θ_j and θ_{j+1}, we divide $\theta_{j+1} - \theta_j$ into p equal spaces. The diffraction pattern at $\theta_{j+q/p} (q < p)$ can be calculated as:

$$I(\theta_{j+q/p}) \;=\; \mathcal{A}\left(\frac{\Delta x\,sin(\theta_1 - \theta_{j+q/p})}{\lambda}\right)^2 \left|\sum_{i=-(N/2-1)}^{N/2} \mathbf{E}_i\; e^{\imath\frac{2\pi\,i\,(j+q/p)}{N}}\right|^2 \qquad (q = 0, 1, 2, \ldots, p-1) \tag{57}$$

$$\;=\; \mathcal{A}\left(\frac{\Delta x\,sin(\theta_1 - \theta_{j+q/p})}{\lambda}\right)^2 \left|\sum_{i=-(N/2-1)}^{N/2} \left(\mathbf{E}_i e^{\imath\frac{2\pi iq/p}{N}}\right)\; e^{\imath\frac{2\pi ij}{N}}\right|^2 \tag{58}$$

So instead of one Fourier transform equation on $\mathbf{E}_i$, we need do p Fourier transform equations on $\mathbf{E}_i\, e^{\imath\frac{2\pi iq/p}{N}}$. Usually, $p = 8$ is sufficient to calculate very nice Fraunhofer diffraction patterns. Eq. (58) is the final scattering formula. It maps the field on the surface, $\mathbf{E}(\mathbf{x})$, to the field intensity of scattering, $I(\theta)$.

C.5. Normalization

Now let's derive the normalization factor $\mathcal{A}$ introduced in Eq. (55). Let ε be the energy carried by each of the N incident rays of the plane wave $\mathbf{E}_1$. The total incident energy, $\mathcal{E}_i$, total reflected energy on the surface, $\mathcal{E}_r$, and the total scattered energy, $\mathcal{E}_s$, are:

$$\mathcal{E}_i \;=\; N\varepsilon \tag{59}$$

$$\mathcal{E}_r \;=\; \sum_{i=-(N/2-1)}^{N/2} |\mathbf{E}_i|^2 \;=\; \varepsilon \sum_{i=-(N/2-1)}^{N/2} A_i^2\,B_i^2\,\left|R(\theta_1 + tan^{-1}(h_i'))\right|^2 \tag{60}$$

$$\mathcal{E}_s \;=\; \int d\theta\, I(\theta) \;=\; \mathcal{A}\int d\xi\,|\mathbf{E}(\xi)|^2 \tag{61}$$

Define the reflectivity of the rough surface as:

$$\mathcal{R} \;\equiv\; \frac{\mathcal{E}_r}{\mathcal{E}_i} \;=\; \frac{1}{N}\sum_{i=-(N/2-1)}^{N/2} A_i^2\,B_i^2\,\left|R(\theta_1 + tan^{-1}(h_i'))\right|^2 \tag{62}$$

Let $\mathcal{E}_r = \mathcal{E}_s$. We obtain:

$$\mathcal{A} \;=\; \frac{\varepsilon\sum_{i=-(N/2-1)}^{N/2} A_i^2\,B_i^2\,\left|R(\theta_1 + tan^{-1}(h_i'))\right|^2}{\int d\xi\,|\mathbf{E}(\xi)|^2} \;=\; \frac{\varepsilon N\mathcal{R}}{\int d\xi\,|\mathbf{E}(\xi)|^2} \;=\; \frac{\mathcal{E}_i\mathcal{R}}{\int d\xi\,|\mathbf{E}(\xi)|^2} \tag{63}$$

ACKNOWLEDGMENTS

This work is supported by NASA Grant NAG8-1607.

REFERENCES

1. L. Rayleigh, *The Theory of Sound*, Macmillan, New York, 1877.
2. P. Beckmann and A. Spizzichino, *The Scattering of Electromagnetic Waves from Rough Surfaces*, Pergamon Press, Oxford, England, 1963.
3. J. A. Ogilvy, *Theory of Wave Scattering from Random Rough Surfaces*, IOP Publishing, Bristol, UK, 1991.
4. L. P. van Speybroeck, D. Jerius, R. J. Edgar, T. J. Gaetz, and P. Zhao, "Performance expectation versus reality," in *Grazing Incidence and Multilayer X-ray Optical Systems*, Hoover and Walker, eds., *Proc. SPIE* **3113**, p. 89, 1997.
5. P. Zhao, L. M. Cohen, and L. P. van Speybroeck, "AXAF HRMA mirror ring focus measurements," in *Grazing Incidence and Multilayer X-ray Optical Systems*, Hoover and Walker, eds., *Proc. SPIE* **3113**, p. 106, 1997.
6. P. Zhao *et al.*, "AXAF mirror effective area calibration using the C-continuum source and solid state detectors," in *X-Ray Optics, Instruments, and Missions*, Hoover and Walker, eds., *Proc. SPIE* **3444**, p. 234, 1998.
7. P. B. Reid, "Fabrication and predicted performance of the Advanced X-ray Astrophysics Facility mirror ensemble," in *X-ray and Extreme Ultraviolet Optics*, Hoover and Walker, eds., *Proc. SPIE* **2515**, p. 361, 1995.
8. P. Zhao and L. P. van Speybroeck, "AXAF VETA-I mirror x-ray test results cross check with the HDOS metrology data," in *X-ray and Extreme Ultraviolet Optics*, Hoover and Walker, eds., *Proc. SPIE* **2515**, p. 391, 1995.
9. cf. W. H. Press, S. A. Teukolsky, W. T. Vetterling, and B. P. Flannery, *Numerical Recipes in C: The Art of Scientific Computing*, Cambridge University Press, Cambridge, 1993.